Wind-Driven Thermocline Variability in the Pacific: A Model–Data Comparison

JOANN LYSNE AND CLARA DESER

National Center for Atmospheric Research, Boulder, Colorado

(Manuscript received 29 March 2001, in final form 25 October 2001)

ABSTRACT

The spatial and temporal patterns of interannual temperature variability within the main thermocline (200–400-m depth) of the Pacific (30°S–60°N) during 1968–97 are documented in two observational datasets and an ocean general circulation model forced with observed winds and air temperatures. Analysis of the processes responsible for the subsurface temperature variance is used to verify the performance of the model and as a basis for assessing the realism of the two observational archives. The subsurface temperature variance is largest in the western portion of the basin, with maxima along the Kuroshio Current Extension and along the equatorward flanks of the subtropical gyres in both hemispheres. In the latter regions, approximately half of the temperature variability may be attributed to local wind-induced Ekman pumping fluctuations one season earlier. A contribution from westward-propagating Rossby waves is also evident in the band 10°–20°N. In contrast, subsurface temperature fluctuations along the Kuroshio Current Extension exhibit little relation to local Ekman pumping variations. Rather, they are linked to basin-scale wind stress curl changes ~4 yr earlier. Similarities and differences between the two observational subsurface temperature archives are discussed.

1. Introduction

The oceans play a crucial role in the climate system by not only transporting heat from low to high latitudes, but also by storing large amounts of energy relative to the atmosphere. This ''reserve'' of heat then acts to regulate the thermal inertia of the climate system. Variations in the heat storage of the ocean are manifest as anomalies in the subsurface temperature field that, in turn, are related to changes in the structure of the upper ocean. In particular, variability in the depth of the thermocline reflects in part the dynamical response of the ocean to fluctuations in the overlying wind field.

The simplest mechanism by which wind stress affects thermocline depth is through Ekman pumping (cf. Gill 1982). In this process, cyclonic (anticyclonic) wind stress curl causes divergence (convergence) of the local Ekman currents that, in turn, induces upwelling (downwelling) beneath the Ekman layer, thereby affecting the depth of the thermocline, or equivalently, temperature at a fixed depth within the thermocline. Westward-propagating Rossby waves may also be generated by Ekman pumping that, in turn, can impact the depth of the thermocline in regions remote from the wind forcing. For timescales longer than the Rossby wave transit time, the wind-driven gyre circulation achieves a quasi-equilibrium with the basin-scale wind stress curl forcing, a state termed ''Sverdrup balance'' (Sverdrup 1947). Although the relevance of Sverdrup theory is questionable in ocean basins such as the North Atlantic where interaction of the flow with bottom topography, thermohaline effects, and inertial and recirculation components play important roles (cf. Wunsch and Roemmich 1985), the large-scale wind-driven circulation in the North Pacific has been shown to be well described by simple Sverdrup dynamics (cf. Niiler and Koblinsky 1985; Qiu and Joyce 1992; Hautala et al. 1994; Kagimoto and Yamagata 1997).

In the first comprehensive study of thermocline depth variability in the northern Tropics based upon historical upper-ocean temperature profiles, Kessler (1990) demonstrated that local Ekman pumping and Rossby wave propagation are the primary mechanisms for interannual thermocline fluctuations (the contribution from Kelvin wave reflection at the eastern boundary is minor). In a more limited study over the southwestern Tropics, Delcroix and Henin (1989) showed that local Ekman pumping variations are responsible for approximately half of the interannual variability in thermocline depth; other processes were not investigated. Using data from biannual hydrographic surveys conducted by the Japanese Meteorological Agency in the western Pacific, Qiu and Joyce (1992) found high correlations between interannual fluctuations of the North Equatorial Current (7°–25°N) and Sverdrup transports estimated from the basinwide wind stress curl field, with the implication that Sverdrup balance is achieved in less than 6 months. The adjustment of the thermocline to wind stress curl var-

Corresponding author address: Dr. Clara Deser, Climate and Global Dynamics Division, NCAR, P. O. Box 3000, Boulder, CO 80307.
E-mail: cdeser@ucar.edu

© 2002 American Meteorological Society

iations in midlatitudes is expected to be slower than in the Tropics due to the decreasing Rossby wave group velocity with increasing latitude (cf. Chelton and Schlax 1996). Recent studies by Miller et al. (1998) and Deser et al. (1999) have shown that observed decadal-scale transport fluctuations of the Kuroshio Current Extension near 40°N lag those inferred from fluctuations in the basinwide wind stress curl field by 4–5 yr, a delay in qualitative agreement with Rossby wave theory.

This investigation focuses on the structure and mechanisms of interannual temperature variability within the main thermocline throughout the Pacific basin (30°S–60°N). We examine an ocean general circulation model hindcast simulation forced by observed atmospheric fields, and two observational subsurface temperature datasets, over the period 1968–97. A particular goal of this study is to verify aspects of the model simulation by comparing the spatial and temporal patterns of thermocline variability with the observational estimates within a framework of simple dynamical constraints on the relation between wind stress curl forcing and thermocline response. We analyze the last 30 yr (1968–97) of a 40-yr hindcast integration of the ocean component of the National Center for Atmospheric Research (NCAR) Climate System Model forced with observed time-varying winds and air temperatures. For the observational ''verification,'' we consider two widely used archives of subsurface temperature profiles to provide a more robust estimate of observed thermocline variability: the Scripps Institute of Oceanography Joint Environmental Data Analysis Center (White 1995) and the *World Ocean Atlas 1998* (Levitus et al. 1998). Our focus on subsurface temperature fluctuations (200–400-m depth) rather than those at the sea surface (or, equivalently, within the mixed layer) reflects that sea surface temperatures are not independent of the parameters used to force the model (in particular, observed surface air temperatures). The use of two observational products for model verification is motivated by the knowledge that the subsurface temperature data are sparse and therefore the method of objective analysis, which differs considerably between the two products, may strongly influence the final results. As far as we are aware, this is the first study to provide a systematic comparison of two widely used subsurface temperature datasets. Another goal of this study is to examine the extent to which simple dynamical mechanisms such as Ekman pumping, Rossby wave propagation, and Sverdrup balance govern the observed and simulated thermocline variability on interannual and longer timescales. The model and observational datasets are described in section 2, the results presented in section 3, and summarized in section 4.

2. Data and methods

a. NCAR ocean model

The simulated subsurface temperature field used in this study is from a 40-yr uncoupled integration of the ocean component of the NCAR Climate System Model (NCOM) described by Doney et al. (2001, manuscript submitted to *J. Climate*). The model is global, with a resolution of 2.4° in longitude, variable resolution in latitude (expanding from ~0.6° at the equator to 1.2° poleward of 30°), and variable resolution in depth (expanding from ~10 m in the upper 50 m to ~40 m at 300–400-m depth, with 20 out of 45 levels in the upper 400 m). The model physics are based upon the Geophysical Fluid Dynamics Laboratory Modular Ocean Model, updated to include an isopycnal mesoscale eddy flux parameterization (Gent and McWilliams 1990) and a nonlocal planetary boundary layer parameterization (Large et al. 1994). Additional details may be found in Gent et al. (1998). The model is forced with momentum, heat, and freshwater fluxes over the period 1958–97 derived from bulk formulas. The inputs to the bulk formulas include 6-hourly 10-m wind, surface air temperature, and relative humidity fields from the National Centers for Environmental Prediction (NCEP) reanalysis product (Kalnay et al. 1996), as well as satellite data products for solar insolation, cloud cover, and precipitation (see Gent et al. 1998 for details). The model is first integrated under repeating annual cycle forcing until it has reached a quasi-equilibrium state. The 40-yr integration is then carried out and repeated for a second cycle to reduce model drift. We analyze data from the second 40-yr integration. Because the simulated sea surface temperature is not independent of the surface forcing due to the fast equilibration between surface air and sea surface temperatures, we restrict the model–data comparison to temperatures below the winter mixed layer in the main thermocline (200–400-m depth).

b. Observed subsurface temperature data

Observational analyses of basin-scale subsurface temperature variability are restricted by the limited data coverage in both space and time. In general, the North Pacific is relatively well sampled compared to the South Pacific, with almost no data available for the Southern Ocean (cf. Tourre and White 1995; Deser et al. 1996; Levitus et al. 1998; Giese and Carton 1999). Although both the observed and model datasets used in this investigation begin earlier than 1968, we choose to analyze the period 1968–97 when the observational data coverage is relatively high in the main thermocline (200–400-m depth).

Due to the paucity of subsurface temperature observations, it is difficult to map the data onto a regular grid without the aid of an objective analysis scheme. Two gridded analysis products of subsurface temperatures were available to us for study: the Scripps Institute of Oceanography Joint Environmental Data Analysis Center archive (hereafter refered to as the SIO dataset; White 1995) and the *World Ocean Atlas 1998* archive produced at the National Ocean Data Center (hereafter refered to as the WOA98 dataset; Levitus et al. 1998). Although the two datasets share a majority of observations, their objective analysis schemes differ considerably. Given the relative paucity of subsurface temperature measurements in both space and time, the different methods of quality control, gridding, objective analysis, and infilling of missing data can have a large impact upon the final product. For this reason, we compare in a systematic fashion the model results against both versions of ''observed'' data. In so doing, we also compare the two observational datasets against one another: this aspect is, as far as we are aware, unique to our study.

The SIO compilation consists nominally of all available temperature profiles from the period 1955–98. As discussed in White (1995), these have been quality controlled and optimally interpolated onto a 2° latitude by 5° longitude grid at each standard level between the surface and 400-m depth. The objective interpolation scheme used to fill in missing data employs a decorrelation length scale of 5° in latitude and 10° in longitude and a decorrelation timescale of 90 days. At any given grid point, gaps in the time series covering less than 20% of the total length of the record were filled by maximum entropy spectral analysis.

The WOA98 archive consists nominally of all available temperature profiles from the period 1948–98. A detailed list of data processing procedures may be found in Antonov et al. (1998). Briefly, initial quality control on all profiles includes duplicate elimination, range and gradient checks, statistical outlier and static stability checks. The quality-controlled data are then interpolated onto standard depth levels using a variable depth tolerance range, and objectively analyzed onto a 1° latitude by 1° longitude grid using the weighting function of Barnes (1973) with a fixed radius of influence of 555 km.

c. *Wind stress curl*

We make use of wind stress curl fields from the NCEP reanalyses as well as from the Florida State University (FSU; Legler and O'Brien 1988). The FSU product, on a 2° latitude by 2° longitude grid for the global Tropics (30°N–30°S), is given in terms of a ''pseudostress'' where the product of the surface air density and the surface drag coefficient have been omitted. Here we have used nominal values of 1.2 kg m^{-3} for air density and 1.3×10^{-3} for the drag coefficient. Differences between these parameters and those used to form the NCEP wind stress product are small compared to differences in the wind fields themselves from the two datasets.

d. *Methods*

The subsurface temperature and wind stress curl datasets were interpolated to the NCEP T42 Gaussian grid (roughly equivalent to 2° lat by 2° lon) for consistency. Monthly anomalies are defined as the departure of the value in a given month and year from the climatological value for that month based upon the period 1968–97. Seasonal and annual anomalies are formed by averaging the monthly anomalies. A variety of simple analysis methods are used, including linear regression and correlation. To evaluate the statistical significance of correlation coefficients, a two-tailed *t* test is used taking into account the effective degrees of freedom in the time series due to temporal autocorrelation following Trenberth (1984). Singular value decomposition is employed in section 3c.

3. Results

a. *Basinwide analyses*

The spatial patterns of interannual temperature variance at two representative depths within the main thermocline (200 and 400 m) are shown in Fig. 1 for the model and the two observational datasets, based on annual anomalies during 1968–97. At both levels, the thermal variability exhibits a zonally banded westward-intensified structure, with maxima in the Tropics of both hemispheres near 10°–20° and along approximately 40°N. The variance maxima are generally more meridionally confined in the model than in the observations. At 200 m, the model overestimates the variability in the central northern subtropics southwest of Hawaii (2 vs 0.4 K^2), and the variability maximum east of Japan is located several degrees poleward of that in the observations. At 400 m, the magnitudes of the subtropical variance maxima in the model are comparable to the observations (0.1–0.2 K^2), but the variability east of Japan is substantially underestimated (0.2 K^2 in the model vs 1 K^2 in the observations). The two observational estimates of thermal variance are generally comparable except at 200 m in the southern subtropics where the values are nearly twice as large in WOA98 compared to SIO. The temperature variance maps based upon WOA98 exhibit more small-scale ''noise'' than those based on SIO, due presumably to the lesser amount of spatial and temporal smoothing in the objective analysis technique.

A comparison of the spatial patterns of interannual variance to the mean temperature structure (Fig. 2) reveals that the regions of maximum variability coincide with the strongest north–south gradients in the mean temperature field in both the model and observations. Since the latitudinal boundaries of the wind-driven gyre circulations are delineated by meridional gradients in the mean thermal field by virtue of thermal wind balance, the variance maxima are indicative of north–south shifts in the gyre boundaries. (Note that this does not necessarily imply that the subsurface temperature fluctuations result from anomalous meridional advection.) Differences between the simulated and observed vari-

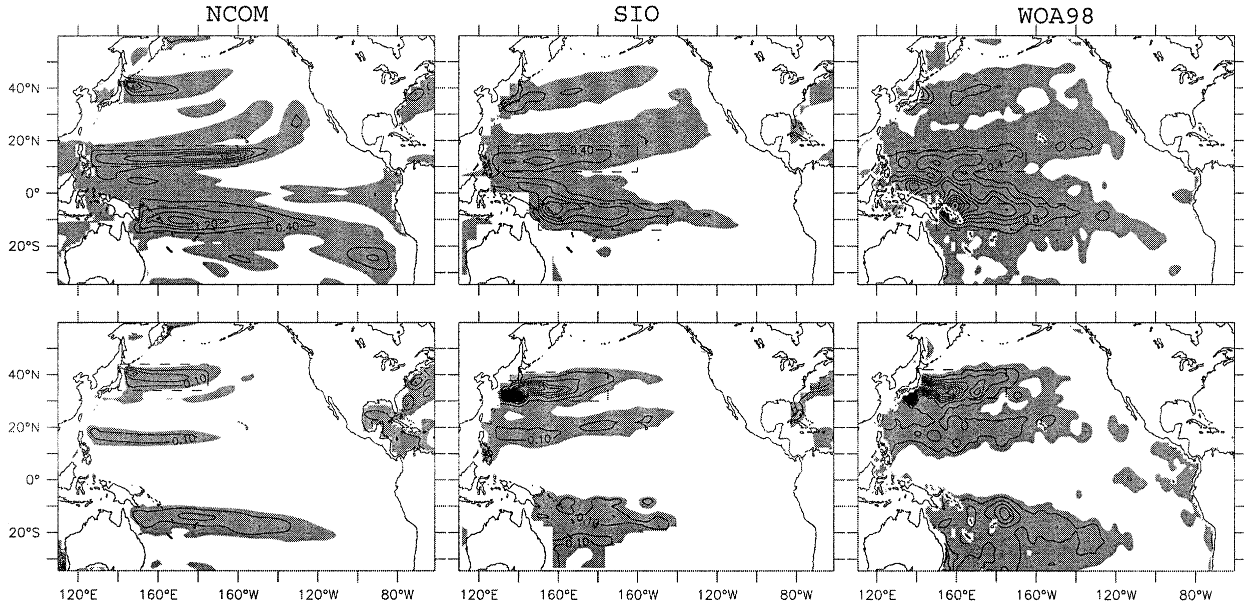

FIG. 1. Interannual temperature variance (K^2) at (top) 200 m and (bottom) 400 m from the (left) NCOM model, (middle) SIO observations, and (right) WOA98 observations based on the period 1968–97. The contour interval is 0.4 K^2 at 200 m and 0.1 K^2 at 400 m. Shading denotes values greater than 0.1 K^2 at 200 m and 0.05 K^2 at 400 m. Dashed rectangles at 200 m show the regions used to define the NW and SW Tropic indices. Dashed rectangles at 400 m denote the regions used to define the North Pacific index.

ability noted above may be understood in terms of differences in the mean temperature structure. For example, the northward displacement and relative weakness of the simulated temperature variability east of Japan at 400-m depth is consistent with the poleward shift and diffuseness of the mean meridional temperature gradient. On the other hand, it is difficult to reconcile the enhanced variability at 200 m in the model south of Hawaii with the background state since the mean thermal gradient is weaker in the model than in the observations.

As discussed in the introduction, wind stress curl plays a central role in controlling the depth of the thermocline. As background to the examination of wind stress curl variations and their relation to temperature fluctuations within the thermocline, Fig. 3 shows the

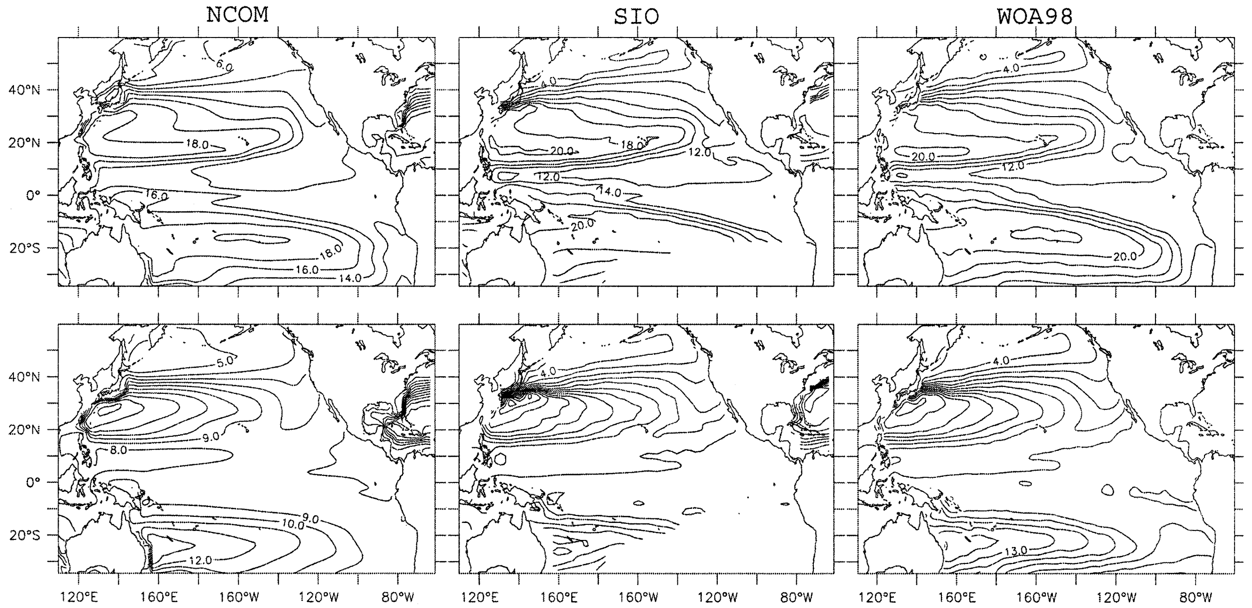

FIG. 2. Climatological mean temperature (K) at (top) 200 m and (bottom) 400 m from the (left) NCOM model, (middle) SIO observations, and (right) WOA98 observations based on the period 1968–97. The contour interval is 2 K at 200 m and 1 K at 400 m.

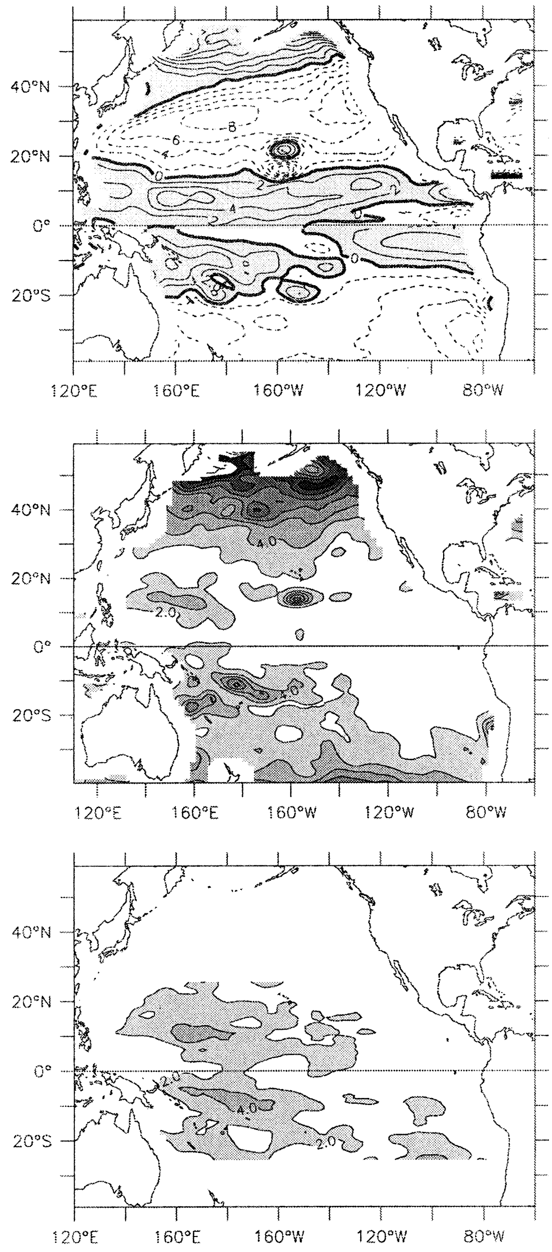

FIG. 3. (top) Climatological wind stress curl (dyn cm^{-3} × 10^{-9})^2 based upon NCEP reanalyses during the period 1968–97. Note that values in the Southern Hemisphere have been multiplied by minus 1 so that positive (negative) values are indicative of cyclonic (anticyclonic) curl in both hemispheres. Interannual variance of wind stress curl (dyn cm^{-3} × 10^{-9}) from (middle) NCEP and (bottom) FSU. Note that FSU winds cover the Tropics only.

mean distribution and interannual variance of annual wind stress curl from NCEP; interannual variance based upon the FSU product is also shown for comparison. The mean wind stress curl (Fig. 3, top) is anticyclonic (negative values) in the subtropics (20°–40°) of both hemispheres, and cyclonic (positive values) in regions of deep atmospheric convection associated with the intertropical convergence zone (ITCZ; ~5°–15°N) and the South Pacific convergence zone (SPCZ; located directly east of New Guinea and northern Australia). The impact of the Hawaiian Islands (~20°N, 157°W) on the mean wind stress curl distribution is evident as a localized north–south couplet; weaker small-scale features associated with islands in the southwestern subtropics are also apparent. These features are also evident in other wind stress curl climatologies derived from surface marine data (cf. Hellerman and Rosenstein 1983; Harrison 1989), numerical weather prediction models (cf. Trenberth et al. 1990), and satellite records (Milliff and Morzel 2001), but are nearly absent from the FSU product (not shown).

The interannual wind stress curl variance based upon NCEP (Fig. 3, middle) is largest over the extratropical North Pacific, but local maxima also occur over the western portion of the Tropics (~10°–20°) in both hemispheres. The southern tropical variance maximum is roughly coincident with the region of mean cyclonic wind stress curl associated with the SPCZ, while the northern tropical variance maximum is situated along the poleward flank of the mean ITCZ. Both variance extrema exhibit amplitudes comparable or larger than the local climatological values of wind stress curl. The interannual wind stress curl variance field based upon FSU (Fig. 3, bottom) is broadly similar to that from NCEP, with maxima in the western Pacific near 10° latitude in either hemisphere. The tropical variance maxima in FSU are generally broader in scale than those in NCEP, and features associated with island topography evident in NCEP are largely absent from FSU (e.g., the variance maximum directly south of Hawaii and due east of Queensland, Australia). The tropical variance maxima in wind stress curl are roughly coincident with those in 200-m temperature (recall Fig. 1).

Next we examine the vertical and temporal structure of interannual thermal fluctuations within the three regions of maximum variance outlined by the dashed rectangles in Fig. 1 (the regional boundaries are listed in Table 1). Note that slightly different areas are used for each dataset to accommodate differences in the locations of the variance maxima.

b. Northwest and southwest Tropics

1) Thermal variability

The vertical and temporal structure of annual temperature anomalies averaged along the westward and equatorward flank of the northern subtropical gyre, a region hereafter refered to as the NW Tropics, is shown in Fig. 4 for both the model and observations. The mean temperature profiles (Fig. 4, left) exhibit the largest vertical gradient between approximately 75- and 300-m depth. The interannual variability peaks within the upper thermocline, reaching maximum values near 150 m of 0.7 K^2 in the model, 0.4 K^2 in SIO, and 0.8 K^2 in WOA98 (Fig. 4, middle). (Note that the model variance

TABLE 1. Boundaries of regional indicies used in this study.

	Area averaging regions		
	NCOM	SIO	WOA98
Kuroshio Extension	140°E–175°W 34°–44°N	140°E–175°W 30°–41°N	140°E–175°W 31°–42°N
Northwest Tropics	127°E–160°W 10°–18°N	130°E–160°W 8°–18°N	130°E–165°W 8°–16°N
Southwest Tropics	151°E–145°W 5°–15°S	150°E–145°W 4°–14°S	150°E–145°W 4°–14°S

exceeds 1.2 K^2 locally within the region defined as the NW Tropics, a value considerably greater than the maximum local variance in either observational dataset; recall Fig. 1). The variance in the model is distributed over a somewhat broader depth range than the observations, in accord with the more diffusive profile of the mean vertical temperature gradient. The timing of positive and negative anomalies (Fig. 4, right) generally compares well among the three datasets: the temporal correlation between the model and SIO (WOA98) at the depth of maximum variability (150 m) is 0.68 (0.68); the correlation between the two observational time series is 0.97. The largest discrepancy between the modeled and observed temperature records occurs during 1978–81 when the simulated anomalies are strongly negative.

The vertical structure of temperature anomalies averaged over the westward and equatorward flank of the southern subtropical gyre (hereafter refered to as the SW Tropics) are shown in Fig. 5. As in the NW Tropics, the maximum variability is located within the upper portion of the main thermocline near 200-m depth, with peak values of 0.85 K^2 in the model, 0.35 K^2 in SIO, and 0.65 K^2 in WOA98. A pronounced cooling trend or shift is evident in all three datasets, with generally positive anomalies during the 1970s and negative values

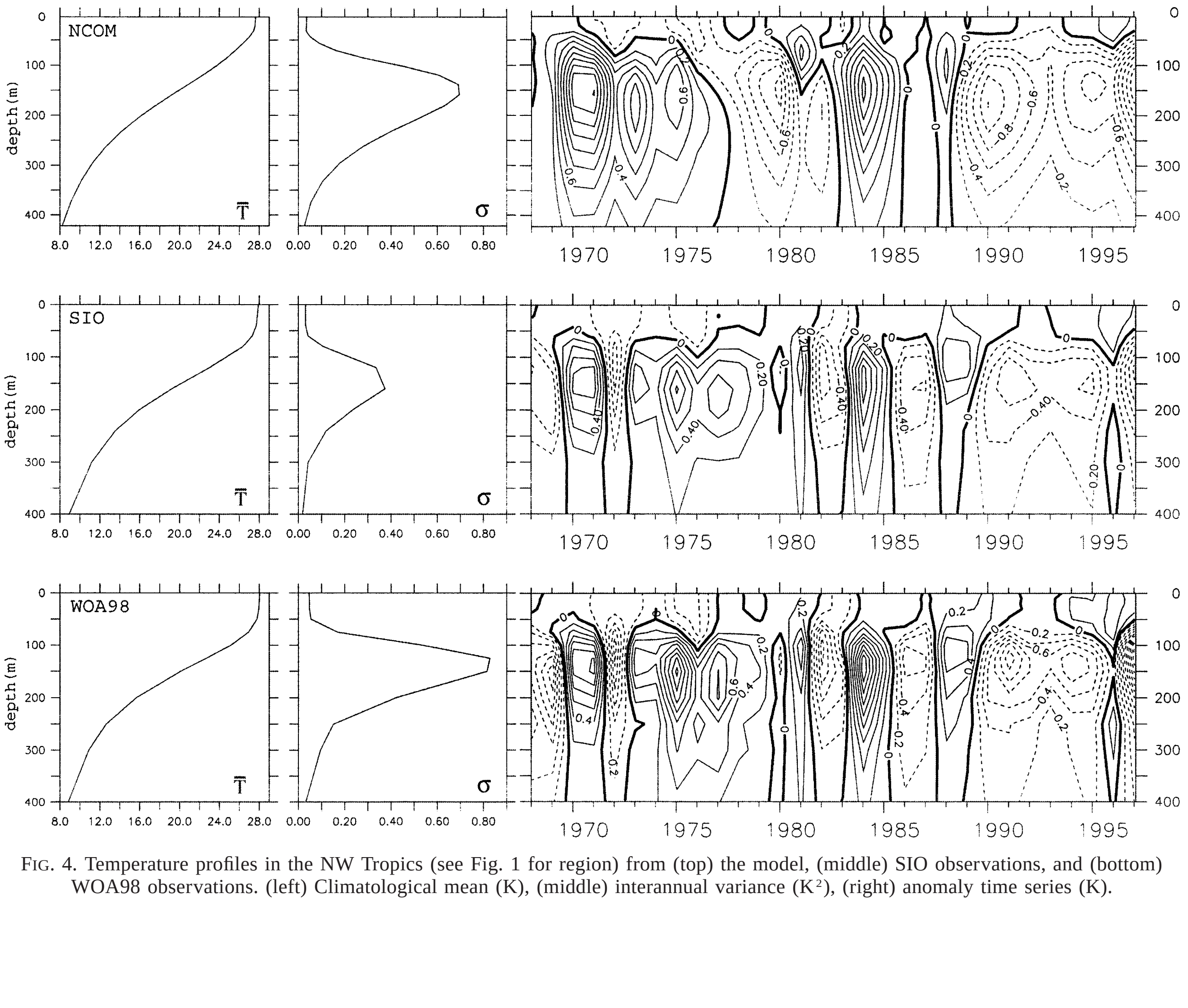

FIG. 4. Temperature profiles in the NW Tropics (see Fig. 1 for region) from (top) the model, (middle) SIO observations, and (bottom) WOA98 observations. (left) Climatological mean (K), (middle) interannual variance (K^2), (right) anomaly time series (K).

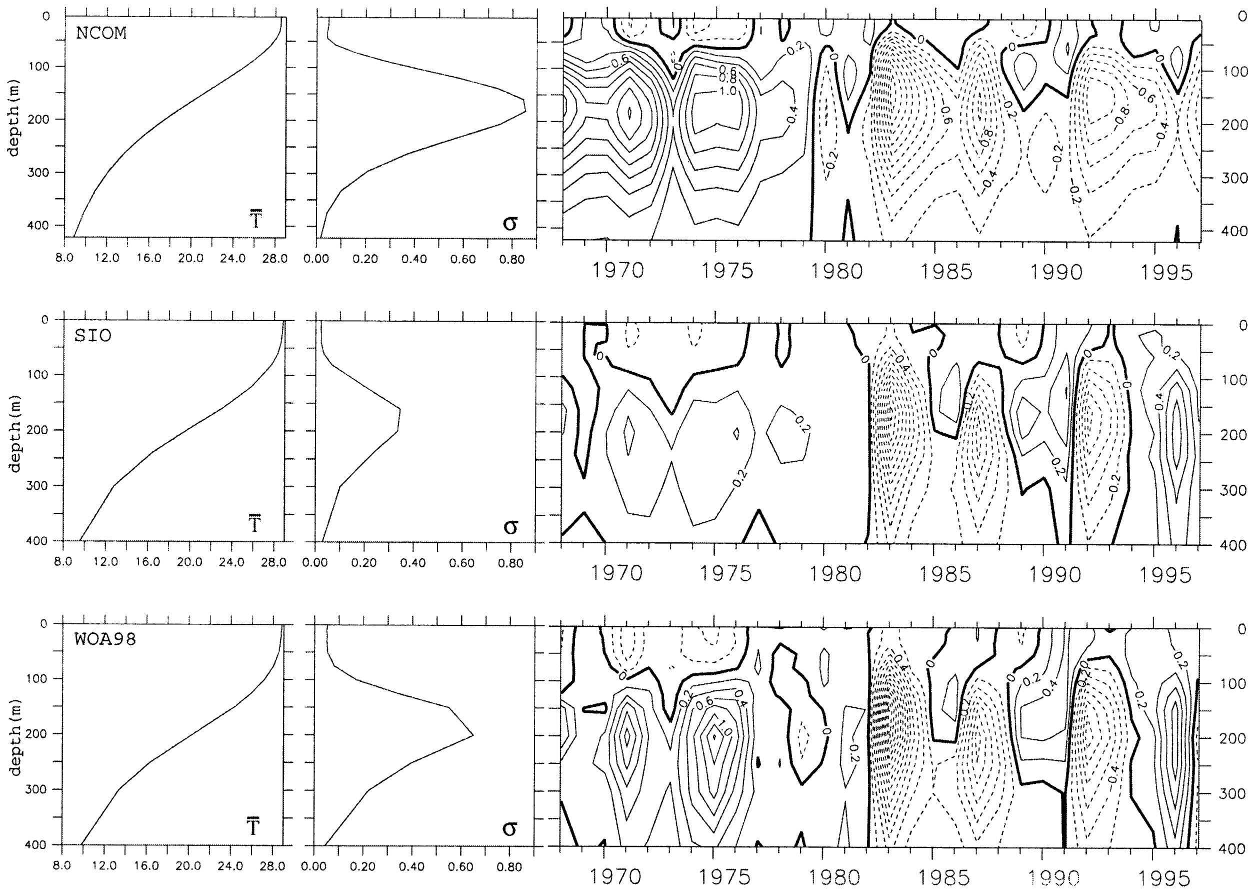

Fig. 5. As in Fig. 4 but for the SW Tropics (see Fig. 1 for region).

during the 1980s and early 1990s. The cooling trend is more pronounced in the model than in the observations due in part to a large positive anomaly in 1968–69 and negative anomalies after 1994. The linear trends over the 30-yr period of record are −2.2 K for the model compared with −0.5 K for WOA98 (SIO exhibits a slight but insignificant positive trend of 0.1 K). A striking feature of Fig. 5 is the weakness of the variability in the SIO data prior to 1980 compared to either the model or WOA98. The temporal correlation between the model and SIO (WOA98) at the depth of maximum variability (200 m) is 0.65 (0.77); the correlation between the two observational time series is 0.92. When the data are detrended, the correlations rise to 0.86 (0.86) between the model and SIO (WOA98), and remain at 0.92 between the two observational records.

2) Relation to local Ekman pumping

The simplest mechanism by which wind stress affects temperature within the thermocline is through Ekman pumping. In this process, a cyclonic (anticyclonic) wind stress curl causes divergence (convergence) of the local Ekman currents that, in turn, induces upwelling (downwelling) beneath the Ekman layer, thereby affecting the depth of the thermocline, or equivalently, the temperature at a fixed depth within the thermocline. The "Ekman" vertical velocity, W_e (positive downward), is given by $[-(1/\rho)\ \mathrm{curl}(\boldsymbol{\tau}/f)]$ where $\boldsymbol{\tau}$ is the surface wind stress vector, f is the Coriolis parameter, and ρ is the density of seawater (taken here as 1025 kg m^{-3}). The temperature change induced by Ekman pumping at a fixed depth h is given by $dT/dt = (-W_e)(dT/dz)$, where T is temperature, t is time, and dT/dz is the vertical temperature gradient at depth h. If we consider anomalies or deviations from the mean seasonal cycle, this balance may be approximated by $dT'/dt = -W_e'\ [dT/dz]$ where the prime denotes anomalies and the square bracket denotes the time-mean seasonal cycle.

To explore the extent to which Ekman pumping is responsible for the temperature variability within the thermocline seen in Figs. 4 and 5, we compare seasonal anomaly time series of temperature at 150 m (200 m) depth for the NW (SW) Tropics and seasonal anomaly time series of Ekman pumping for the same regions. The results are shown in Figs. 6 and 7 for the NW and SW Tropics, respectively. For this calculation we have chosen a consistent area-averaging box (10°–18°N, 140°E–170°W for the NW Tropics and 6°–16°S, 170°E–145°W for the SW Tropics) so that the wind contribution

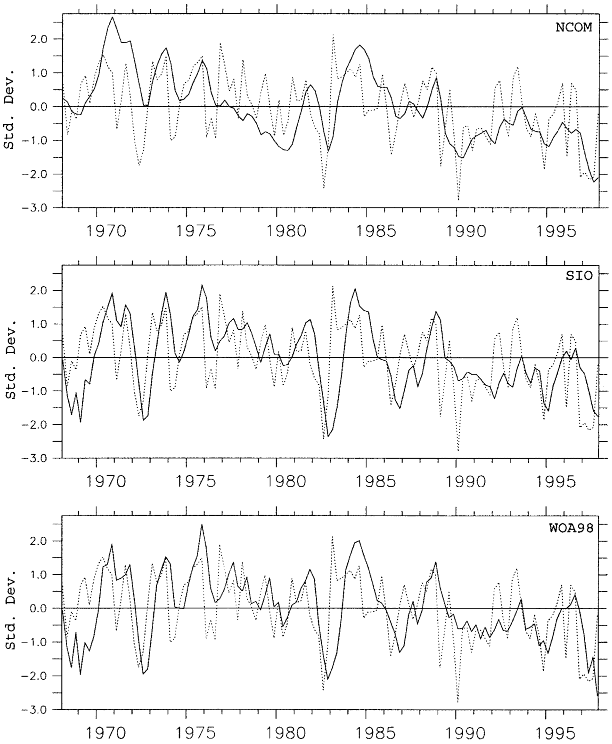

FIG. 6. Normalized time series of seasonal Ekman pumping (dashed curve) and 150-m temperature (solid curve) anomalies for the NW Tropics from (top) the model, (middle) SIO observations, and (bottom) WOA98 observations. No temporal smoothing has been applied. Units are std dev.

is identical for each dataset. There is a close visual correspondence between the time series of anomalous Ekman pumping and thermocline temperature for all three datasets and for both regions, with the atmosphere generally leading the ocean by a season or two. It is also evident that the Ekman pumping record exhibits more high-frequency (subannual) variability than the thermocline time series. The most notable discrepancy between the records of Ekman pumping and thermocline temperature anomalies in the NW Tropics (Fig. 6) occurs in the model during 1977–80 when the simulated temperatures are strongly below normal yet those induced by local Ekman pumping are near zero or slightly positive. Since the observed thermocline temperatures do appear to be consistent with local Ekman pumping during this period, we speculate that the model is unduly influenced by remote processes during this time. We also note that prior to 1980 when the SIO thermocline temperature variability is weak compared to both the model and WOA98 datasets (recall Fig. 5), local Ekman pumping is well correlated with thermocline temperature in both the model and WOA98 observations, a result which lends support to the notion that the SIO data for the SW Tropics prior to 1980 are partially unrealistic.

To quantify the correspondence between the Ekman pumping and thermocline temperature anomaly records shown in Figs. 6 and 7, we have computed correlation coefficients between the two records as a function of time lag from -8 to $+8$ seasons (Fig. 8). The correlations are based upon seasonal detrended anomalies, and the Ekman pumping time series were first lightly smoothed in time with a three-point binomial filter to reduce high-frequency variability present in the wind data. For all 3 datasets and for both regions, the correlations maximize when the atmosphere leads the ocean by 1–2 seasons, with peak values between 0.65 and 0.75. That is, approximately half of the variance in thermocline temperature variability may be accounted for by wind-induced Ekman pumping variations one season earlier. In the NW Tropics, the peak correlations are slightly weaker for the model than for observations. We speculate that this is due to the stronger influence of remote forcing upon thermocline variability in the model than in observations (see below). It may also be noted that for the NW Tropics, the correlations for the observed data are significantly negative at lags -5 to -2 seasons (ocean leading atmosphere). We interpret this feature as a reflection of a biennial component to the observed thermocline and wind stress curl variability that is visually apparent in the raw time series (recall Fig. 6). The lack of a pronounced biennial component to the model correlations reflects the additional contribution of longer timescale events such as that during 1977–80.

3) WESTWARD PROPAGATION

As shown above, approximately half of the variance in thermocline temperatures in the NW and SW Tropics may be accounted for by wind-induced Ekman pumping variations one season earlier. What processes contribute to the remaining portion of thermocline temperature variance? The observational study of Kessler (1990) and the analyses of ocean model simulations by Xie et al. (2000) and Capotondi and Alexander (2001) indicate that westward-propagating first-mode baroclinic Rossby waves influence thermocline variability in the northwestern Tropics, particularly in the latitude band 12°–14°N. These Rossby waves may be generated by anomalous Ekman pumping in the eastern Tropics and by reflection of coastal Kelvin waves at the eastern boundary. To explore the possible role of Rossby waves in interannual thermocline variability in the model and observations, we show in Fig. 9 time–longitude diagrams of seasonal detrended anomalies of the depth of the 20°C isotherm averaged over the latitude band 10°–18°N, the same averaging interval used to define the NW Tropics region, for the model (left), SIO (middle), and WOA98 (right). Here, thermocline depth is approximated by the depth of the 20°C isotherm following Kessler (1990): the mean depth of this isotherm ranges from 150–200 m in the western Tropics to 50–80 m in the east (see Kessler 1990, his Fig. 4). Hovmöller maps for the latitude band 12°–14°N are very similar to those in Fig. 9, although the variability is approximately 30% stron-

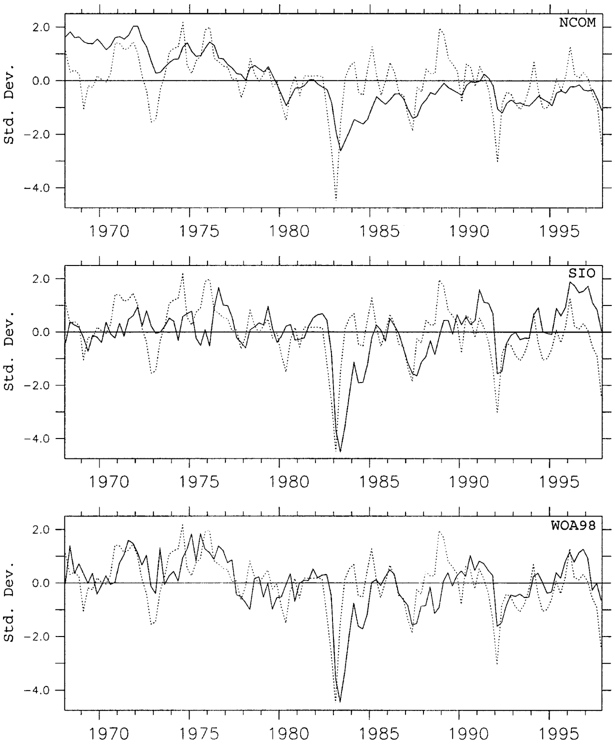

FIG. 7. As in Fig. 6 but for the SW Tropics, where temperatures at 200-m depth are used in place of 150 m.

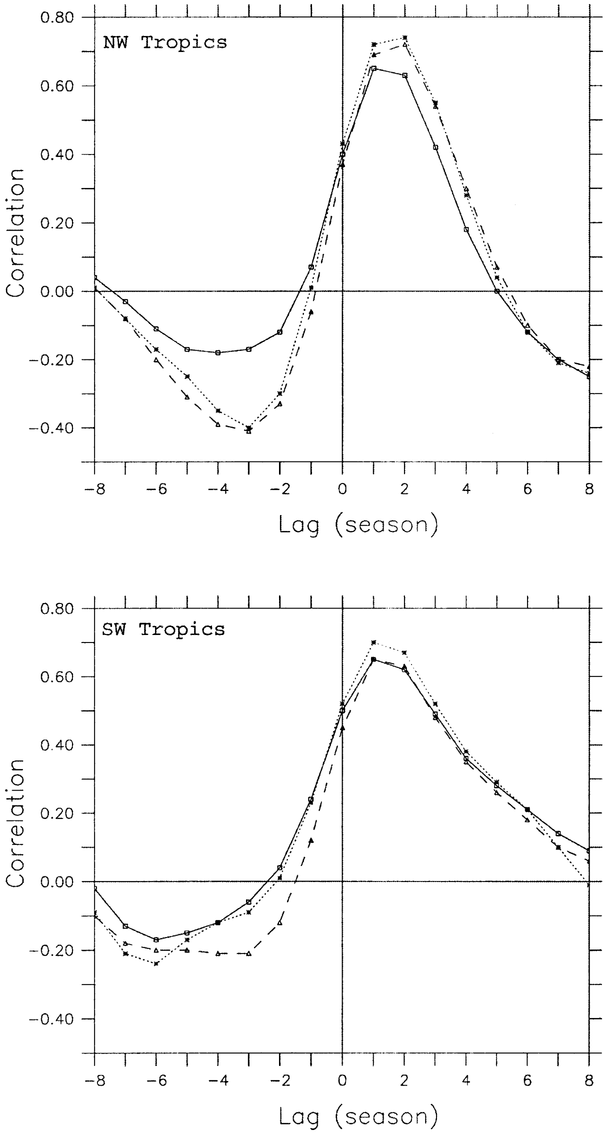

FIG. 8. (top) Lag correlations between the seasonal anomaly time series of Ekman pumping and 150-m temperature for the NW Tropics for the model (solid curve), SIO observations (dashed curve), and WOA98 observations (dotted curve). The Ekman pumping time series were first smoothed in time with a three-point binomial filter. Both the Ekman pumping and temperature records have been detrended. Positive (negative) lags denote Ekman pumping leading (lagging) thermocline temperature. (bottom) As in top, but for SW Tropics; note that temperatures at 200-m depth are used in place of 150-m depth.

ger (not shown). Westward-moving disturbances are evident in all three datasets, some originating at the eastern boundary and others near 130°W; the latter commonly reach the western boundary while the former are often trapped within 20°–30° of the eastern boundary. Individual westward-moving disturbances are well simulated by the model with the notable exception of the propagating negative thermocline depth anomalies during 1977–81 present in the model but not in the observations.

To summarize the character of the westward-moving disturbances evident in the Hovmöller diagrams, we have computed lag correlations between thermocline depth anomalies at the western boundary (140°–150°E average) and thermocline depth anomalies at all other longitudes (Fig. 10). The results show that in both the model and observations, the typical transit time for westward-moving disturbances is approximately 1.5 yr from 140°W to 140°E, or a speed of approximately 18 cm s^{-1}. This is similar to the theoretical phase speed (18–20 cm s^{-1}) of the first baroclinic mode Rossby wave based on the model stratification in the region of interest (Capotondi and Alexander 2001). It should be noted however, that the correlations decay rapidly from the western boundary, with the correlation between thermocline depth anomalies at 140°E and 140°W on the order of 0.3. East of approximately 130°W, the correlation structure differs among the three datasets. In the model, a secondary maximum emanates from the eastern boundary, but extends only 20° into the interior; in the SIO, weak correlations (less than 0.2 in magnitude) are found; in the WOA98, a signal resembling that in the model near the eastern boundary is evident. The complex nature of the correlations east of 130°W is consistent with ones visual impression from the Hovmöller diagrams shown in Fig. 9; namely, that disturbances emanating from the eastern boundary propagate on occasion all the way to the western boundary, but more often decay within approximately 20°–30° of the

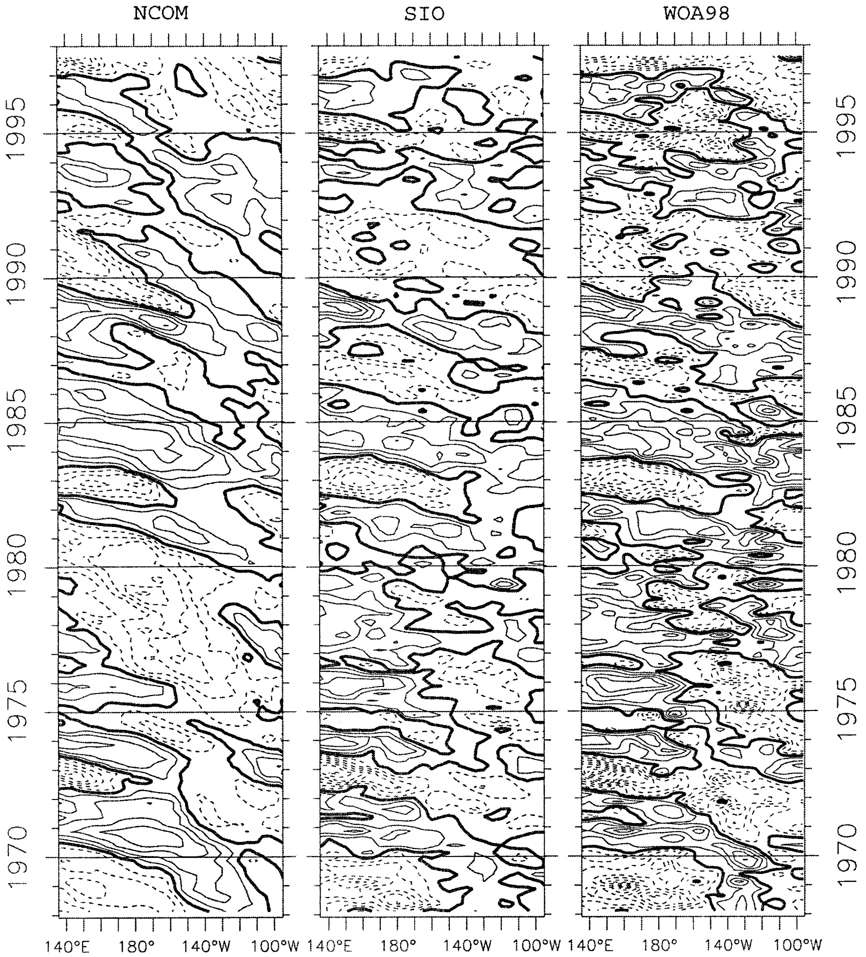

FIG. 9. Time–lon diagram of seasonal anomalies of the depth of the 20°C isotherm averaged over the band 10°–18°N for (left) the model, (middle) SIO observations, and (right) WOA98 observations, based upon seasonal detrended data. Contour interval is 5 m, negative thermocline depth displacements are dashed, and values in excess of 5 m in absolute value shaded.

coast. Another discrepancy between the model and observations is the signature of a quasi-4-yr periodicity in the correlations based on observations (note, e.g., the negative correlations at ± 8 seasons in the west) but not in those based on the model. This quasiperiodicity is also evident in the Hovmöller diagrams (recall Fig. 9). We speculate that the weakness of this feature in the model is due in part to the overly extended duration of individual events (e.g., the negative anomalies during 1977–81, among others; see Fig. 9).

The observed correlations shown in Fig. 10 are comparable to those of Kessler (1990) that were based on bimonthly data during 1970–87. The maximum correlation coefficient in Fig. 10, which occurs at 170°W, exceeds 0.6 in both the SIO and WOA98 datasets compared to 0.5 in Kessler's analysis; considering that our data record is two-thirds longer than Kessler's (30 vs 18 yr), this indicates a high degree of statistical confidence in the results. We have found no evidence for westward-propagating disturbances in the depth of the 20°C isotherm at comparable latitudes in the southern Tropics, although at subtropical latitudes (e.g., 15°–25°S), there is evidence from both the model and observations of westward propagation (not shown).

4) A DISCREPANCY BETWEEN THE MODEL AND OBSERVATIONS

It was noted earlier that there is a strong discrepancy between the simulated and observed thermocline temperature anomalies in the NW Tropics region during 1977–80, and that the simulated anomalies are not consistent with local Ekman pumping, but likely derive from westward-propagating disturbances originating in the eastern portion of the basin (recall Figs. 6 and 9). To examine the origin of this discrepancy, we have formed regional time series of thermocline depth and Ekman pumping anomalies in the area directly east of that used to define the NW Tropics box (10°–18°N, 160°–100°W), hereafter refered to at the NE Tropics

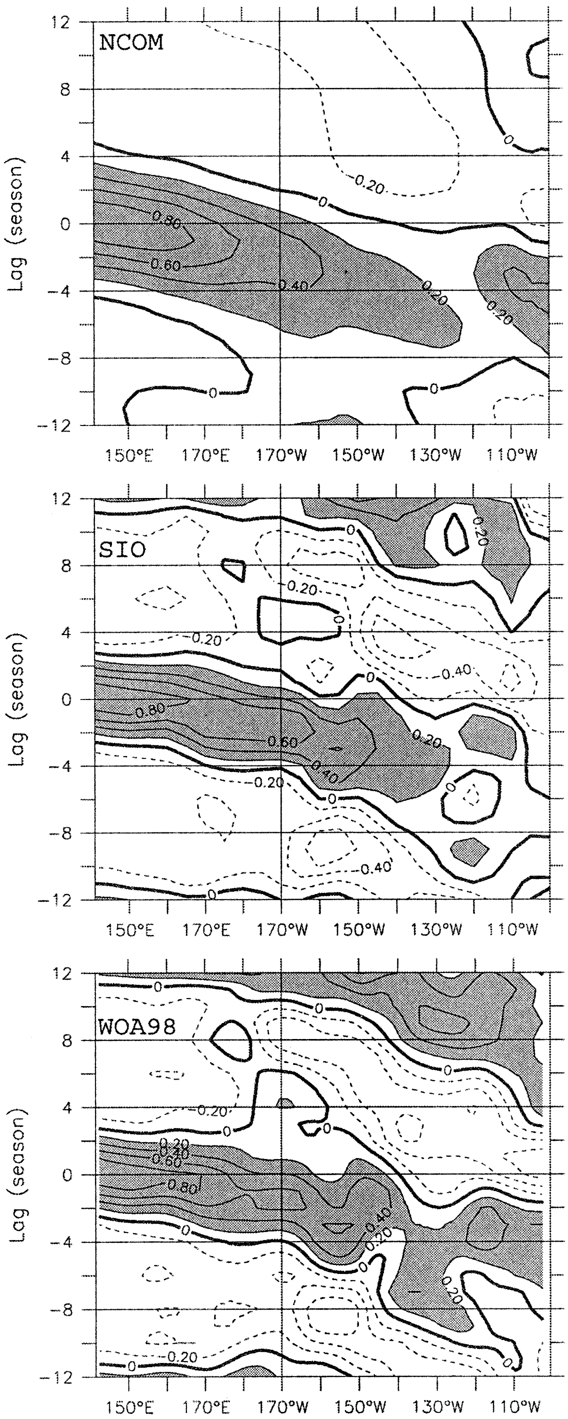

FIG. 10. Lag correlations of seasonal anomalies of the 20°C isotherm depth averaged over the band 10°–18°N near the western boundary (140°–150°E) and all lon to the east for (top) the model, (middle) SIO observations, and (bottom) WOA98 observations. Correlations were performed on the data shown in Fig. 9.

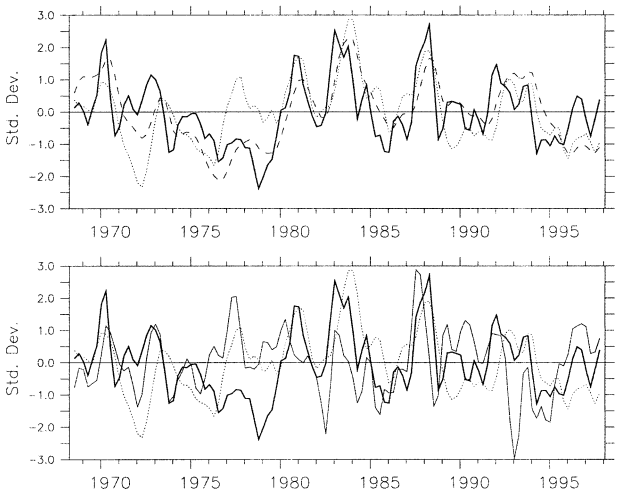

FIG. 11. (top) Time series of seasonal Ekman pumping based upon NCEP reanalyses (thick solid curve) and 20°C isotherm depth from the model (dashed curve) and WOA98 observations (dotted curve) for the NE Tropics (10°–18°N, 160°–100°W). All records are standardized and smoothed with a three-season running mean. (bottom) As in top, but for Ekman pumping based upon NCEP (thick solid curve) and FSU (thin solid curve), and 20°C isotherm depth from WOA98 observations (dotted curve).

(Fig. 11, top). The simulated and observed thermocline depth anomalies are very similar except during 1976–79 when the model exhibits much lower values than the observations. Further, the simulated values during this period are in good agreement with local Ekman pumping anomalies, while the observed thermocline depth anomalies are not. From the Hovmöller diagram of thermocline depth anomalies (Fig. 9), it is seen that negative values originating in the east during the period 1976–79 propagate westward, resulting in a period of negative values in the NW Tropics during 1977–80. Thus, local Ekman pumping in the NE Tropics is responsible for the simulated negative thermocline depth values in the NW Tropics 1–2 yr later.

Why are the observed thermocline depth anomalies not consistent with local Ekman pumping in the east during 1976–79? One possibility is that the Ekman pumping anomalies derived from NCEP are erroneous. To investigate this possibility, we have computed the regional Ekman pumping time series for the NE Tropics region from the FSU dataset. The Ekman pumping time series derived from NCEP and FSU for the NE Tropics are compared in Fig. 11 (bottom). It is clear that the largest discrepancy between the two wind records occurs during 1976–79, with the FSU (NCEP) product consistent with driving the observed (simulated) thermocline depth variations. Although the FSU-derived Ekman pumping anomalies compare favorably with the observed thermocline depth fluctuations during 1976–79, FSU exhibits poorer agreement with the observed thermocline depth variations than NCEP for the period 1968–97 as a whole. The maximum correlations between seasonal, detrended Ekman pumping anomalies

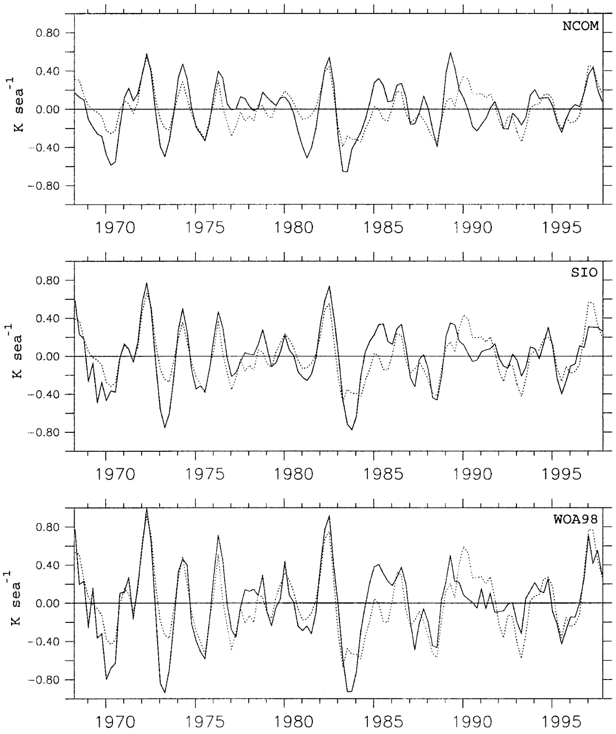

FIG. 12. Time series of seasonal Ekman pumping anomalies multiplied by the long-term mean vertical temperature gradient at 150-m depth (K sea^{-1}; dashed curve) and 150-m temperature anomaly tendency based upon a one-season forward difference (K sea^{-1}; solid curve) for the NW Tropics from (top) the model, (middle) SIO observations, and (bottom) WOA98 observations. A three-season running mean has been applied to all curves.

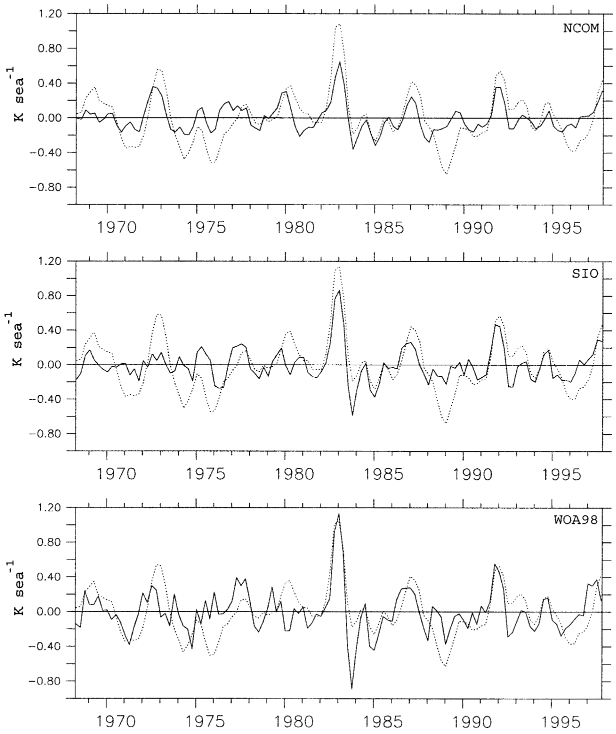

FIG. 13. As in Fig. 12 but for the SW Tropics, where temperatures at 200-m depth are used in place of those at 150 m.

and thermocline depth anomalies in the NE Tropics (which occurs at +1 season lag for all datasets) are −0.06 for the model, 0.11 for SIO, and 0.17 for WOA98 based upon FSU compared to 0.77 for the model, 0.55 for SIO, and 0.52 for WOA98 based upon NCEP. Ekman pumping anomalies in the NW Tropics exhibit close agreement between NCEP and FSU (not shown).

5) TEMPERATURE TENDENCY

In this section, we explore the extent to which local Ekman pumping variations account quantitatively for the thermocline temperature anomaly tendencies in the NW and SW Tropics. Figure 12 (13) compares the anomalous temperature tendency based on a one-season forward difference at 150-m (200 m) depth for the NW (SW) Tropics with the Ekman-induced temperature anomaly based upon NCEP. It is clear from all three datasets that Ekman pumping not only qualitatively, but quantitatively, accounts for much of the one-season temperature tendencies in both regions. The correlations between the actual and Ekman-induced temperature tendencies are 0.72 (0.72) for the model, 0.79 (0.66) for SIO, and 0.80 (0.61) for WOA98 for the NW (SW) Tropics: all exceed the 1% significance level of 0.33. The regression coefficients for the NW Tropics are close to unity (0.96 for both the model and SIO and 0.92 for WOA98), indicating that there is nearly a 1:1 correspondence in amplitude between the actual and Ekman-induced one-season temperature anomaly tendencies. The regression coefficients for the SW Tropics are lower (0.40 for the model, 0.42 for SIO, and 0.55 for WOA98), suggesting that other processes are also important for thermocline temperature anomaly changes. In a more limited study based upon data at point locations within the southwestern tropical Pacific during 1975–85, Delcroix and Henin (1989) found that local Ekman pumping accounted for a similar fraction of the observed interannual thermocline variability to that found here.

c. North Pacific

The region east of Japan along the Kuroshio Current Extension exhibits a local maximum in subsurface temperature variance (Fig. 1). The vertical and temporal structure of thermal anomalies from the model and the two observational datasets averaged over this area (hereafter refered to as NPAC; see Table 1 for the details of the averaging region) is shown in Fig. 14. Compared to the Tropics, the mean stratification is weak (a range of ~8 K over 400 m compared to ~20 K for the Tropics; recall Figs. 5 and 6), and the variance profile is nearly uniform within the upper 400 m, particularly for the observations, with values around 0.1–0.2 K^2. Decadal-

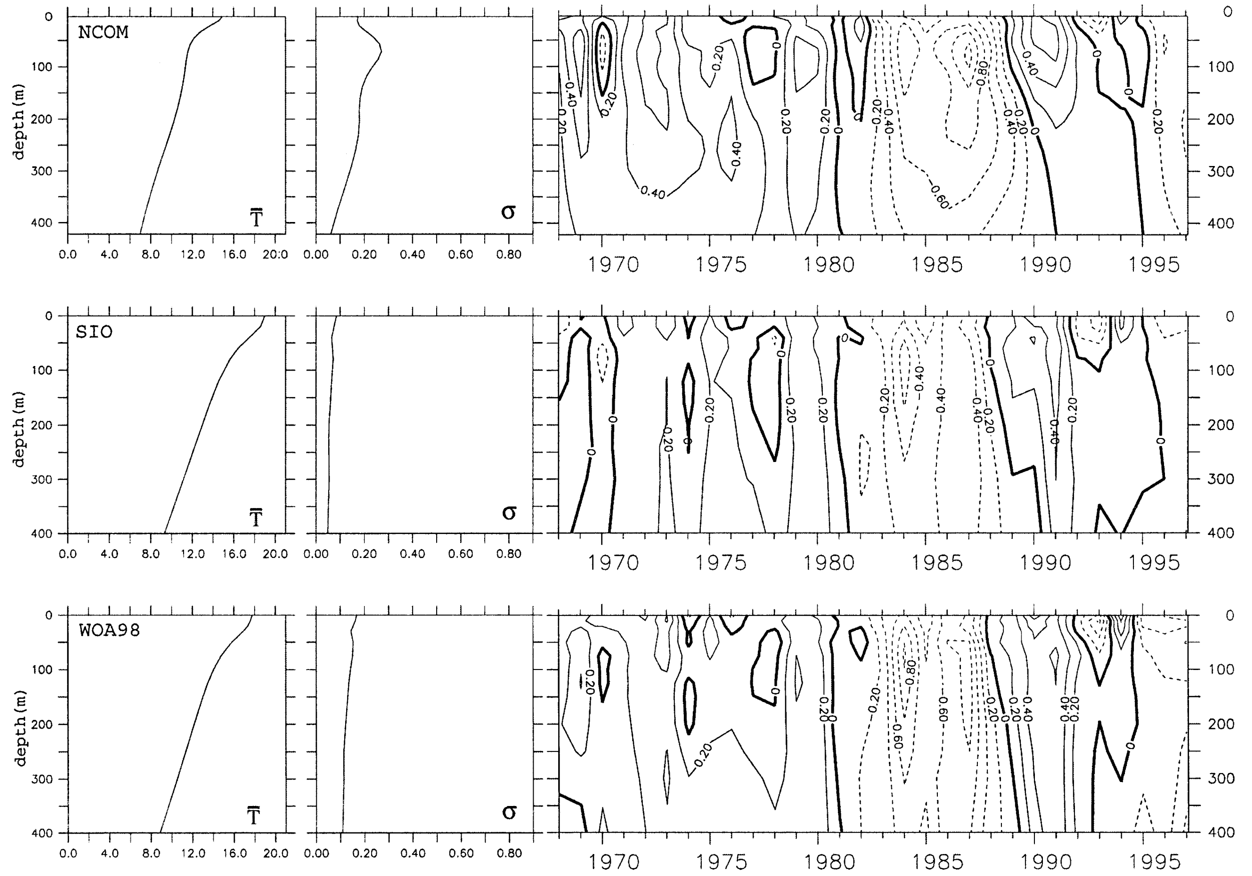

FIG. 14. Temperature profiles in the North Pacific (see Fig. 1 for region) from (top) the model, (middle) SIO observations, and (bottom) WOA98 observations. The mean (K) and variance profiles (K^2) are shown in the left and middle panels, respectively. The time–depth structure of annual temperature anomalies (K) is shown in the right panels.

scale variability is evident in the temperature anomaly time series (Fig. 14, right), with generally warmer than normal conditions in the 1970s, colder conditions in the 1980s, and mixed conditions in the 1990s.

Figure 15 shows seasonal anomaly time series of temperature at 400-m depth in the NPAC region. The simulated 400-m temperature record compares well with the observations, both in amplitude and phase, although the observations exhibit a larger degree of high-frequency variability. The main discrepancies occur in 1990–91 when the observed temperature anomalies are strongly positive but the model is near zero, and in 1969–71 when the simulated anomalies are positive yet the observed ones are near zero. The correlation coefficient between the model and SIO (WOA98) NPAC records is 0.88 (0.86) and that between the two observational time series is 0.91 based on seasonal anomalies smoothed with a three-point running mean.

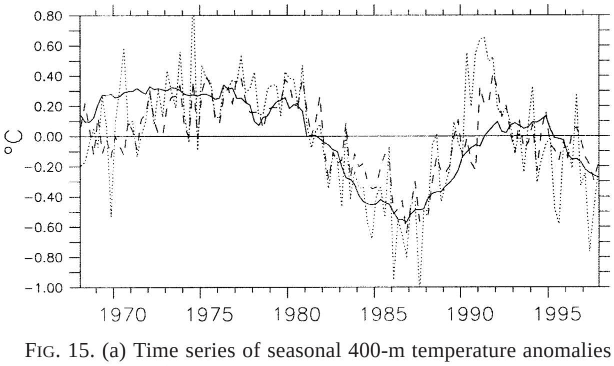

FIG. 15. (a) Time series of seasonal 400-m temperature anomalies in the North Pacific region for the model (solid), SIO observations (dashed), and WOA98 observations (dotted). No temporal smoothing has been applied to any of the curves.

Unlike the NW and SW Tropics, thermocline temperature anomalies in the NPAC region are not significantly correlated with local Ekman pumping anomalies in any of the datasets: correlation coefficients are less than 0.25 for lags between zero and four seasons (atmosphere leading ocean) based upon seasonal anomalies smoothed in time with five-point binomial filter (the correlations are even weaker for unsmoothed data). To explore possible nonlocal relationships between thermocline temperature and wind stress curl anomalies, we have computed regression maps of wind stress curl anomalies at each grid point over the North Pacific upon the 400-m NPAC index

TABLE 2. Statistics associated with the leading mode of an SVD analysis between annual anomalies of wind stress curl and 400-m temperature over the North Pacific during 1968–97 at lags 0–5 yr (atmosphere leading ocean) for the model (NCOM) and observations (SIO and WOA98). (top row) The percent squared covariance; (middle row) the actual squared covariance normalized to unity at zero lag (numbers in parentheses indicate actual squared covariance using data from 1968–89 only); (bottom row) the correlation coefficient between the wind and temperature principal component time series.

	SVD Mode 1						
	Lag 0	Lag 1	Lag 2	Lag 3	Lag 4	Lag 5	
NCOM	68%	69%	71%	72%	73%	69%	% Cov^2
	1.00	1.13	1.18	1.26	1.29	1.16	Norm Cov^2
	(1.00)	(1.21)	(1.32)	(1.48)	(1.57)	(1.54)	Norm Cov^2
	0.47	0.63	0.77	0.87	0.90	0.87	PC Corr
SIO	41%	45%	43%	48%	49%	49%	% Cov^2
	1.00	1.22	1.10	1.28	1.42	1.39	Norm Cov^2
	(1.00)	(1.12)	(1.08)	(1.43)	(1.80)	(1.80)	Norm Cov^2
	0.37	0.58	0.72	0.82	0.88	0.82	PC Corr
WOA98	45%	52%	53%	51%	48%	52%	% Cov^2
	1.00	1.32	1.40	1.33	1.21	1.31	Norm Cov^2
	(1.00)	(1.15)	(1.39)	(1.78)	(2.02)	(1.88)	Norm Cov^2
	0.19	0.46	0.69	0.80	0.88	0.80	PC Corr

for lags −2 to +6 yr (positive lags denote wind leading temperature). The results (not shown) indicate that the largest regression coefficients occur when wind stress curl leads the NPAC index by 3–5 yr and that these wind stress curl regressions are basinwide in extent.

The nonlocal, noncontemporaneous nature of the association between wind stress curl and thermocline variability may be examined more generally using the technique of singular value decomposition (SVD) analysis (cf. Bretherton et al. 1992; Deser and Timlin 1997). Here we have applied SVD analysis to annual wind stress curl and 400-m temperature anomaly fields over the North Pacific (20°–50°N) at lags 0–5 yr (atmosphere leading ocean). This approach provides a quantitative assessment of the strength of the coupling between the wind stress curl and thermocline temperature anomaly fields as a function of time lag, as well as the optimal spatial patterns of covariability (note that a separate SVD analysis is carried out for each lag). As input to the SVD routine, the wind stress curl and temperature anomaly fields were each normalized by their overall variance to ensure equal weighting of the two parameters. In addition, the wind stress curl anomalies were low-pass filtered in time with a three-point binomial filter to reduce high-frequency variability not present in the 400-m temperature field. The results are summarized in Table 2 and illustrated in Fig. 16.

The leading SVD mode accounts for a substantial portion of the covariance between the wind stress curl and 400-m temperature anomaly fields, with values ∼70% for the model, ∼45% for SIO, and ∼50% for WOA98 (Table 2). Note that the percentage covariance accounted for by the leading mode is relatively insensitive to lag; however, the actual covariance exhibits a strong dependence on lag, with the largest values at 4 yr in both the model and SIO datasets and at 2 yr for WOA98 (Table 2). These peak covariances are 29%, 42%, and 40% larger than the values at zero lag for the model, SIO, and WOA98, respectively (Table 2). The temporal correlation coefficients between the PC time series of the wind stress curl and 400-m temperature anomaly patterns for the leading SVD mode maximize at lag 4 yr for all three datasets, with values near 0.9 (note that the zero-lag correlations are considerably weaker at 0.2–0.5). Thus, the strongest temporal coupling between the spatial patterns of wind stress curl and 400-m temperature anomalies associated with the leading SVD mode occurs when the atmosphere leads the ocean by 4 yr.

The spatial patterns and PC time series of wind stress curl and 400-m temperature anomalies associated with the leading SVD mode at lag 4 yr are shown in Fig. 16. The wind stress curl anomaly patterns are consistent among the three datasets, with a north–south dipole with centers along ∼30° and ∼38°N and the strongest anomalies in midbasin (this pattern is nearly identical to that derived by regressing wind stress curl anomalies at each grid point upon the 400-m NPAC temperature index at a lag of 4 yr as mentioned above). The 400-m temperature anomaly patterns are westward intensified, with the strongest center of action east of Japan ∼38°N in the region of the Kuroshio Current Extension in all three datasets. Weaker anomalies occur to the south, but these are not consistent between the model and observations. The PC time series confirm that the transition from positive to negative subsurface temperature anomalies around 1981 in the Kuroshio Extension is associated with an earlier transition (∼1977) in the basinwide wind stress curl pattern. The second zero crossing of the wind stress curl PC in 1988 is followed by a transition in the subsurface temperature PC in 1992 for the model, 1991 for SIO, and 1990 for WOA98. Thus, the temporal lag between the wind stress curl and thermocline temperature PCs is smaller and less consistent for the second zero crossing than for the first. When the second zero crossing is excluded from the SVD analysis by restricting the

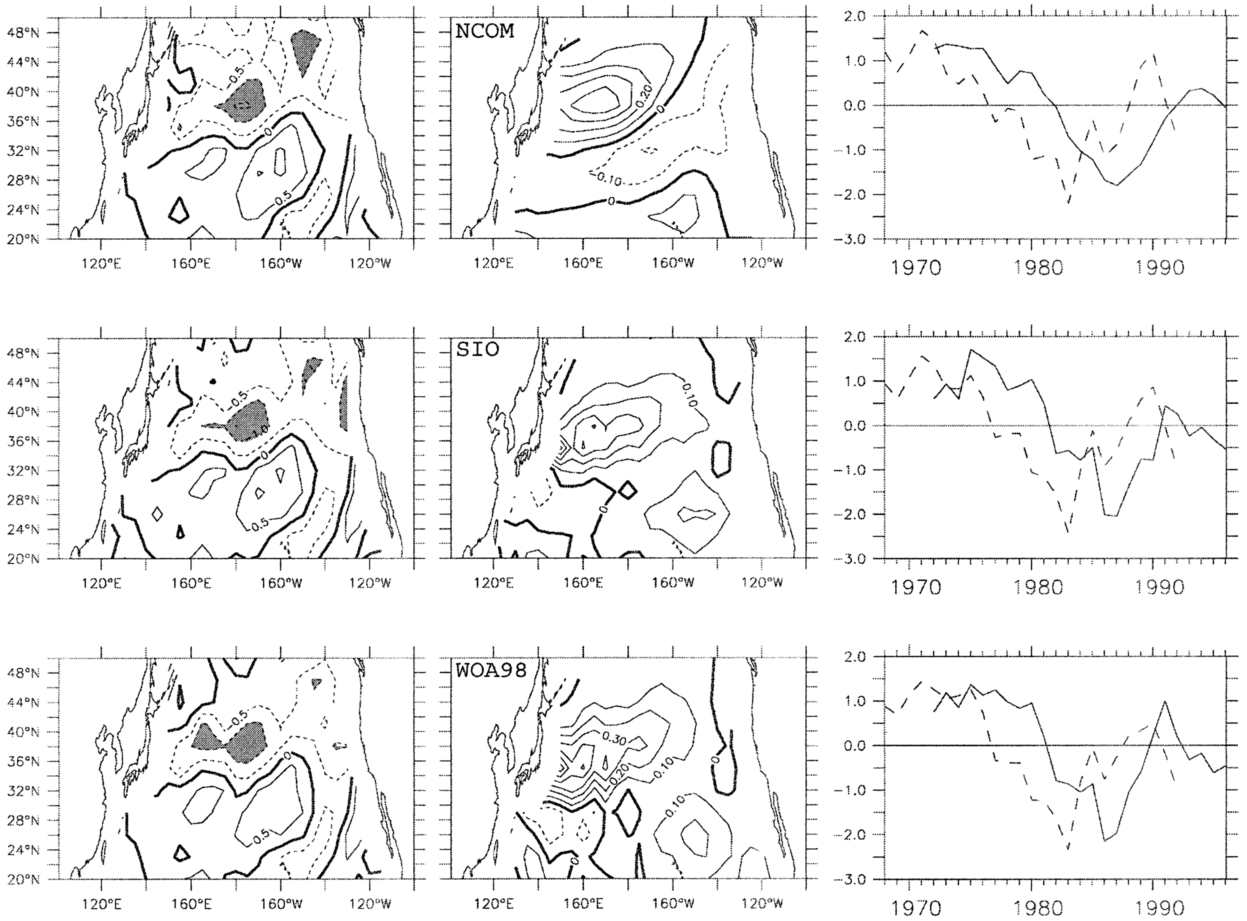

Fig. 16. Leading SVD mode between annual anomalies of wind stress curl and 400-m temperature over the North Pacific at a 4-yr lag (atmosphere leading ocean) from (top) the model, (middle) SIO observations, and (bottom) WOA98 observations. Spatial patterns of wind stress curl and 400-m temperature anomaly fields are shown in the left and middle panels, respectively. Principal component time series of wind stress curl (dashed curve) and 400-m temperature anomalies (solid curve) are shown in the right panel. Additional statistics of this mode are presented in Table 2.

period of record to 1968–89, the largest squared covariances for the leading mode occur at a lag of 4 yr for all three datasets, with a relative enhancement of 57%, 80%, and 100% compared to zero lag for the model, SIO, and WOA98, respectively (Table 2). The spatial patterns and PC time series are nearly identical to those based on the full period of record (not shown).

The spatial patterns and temporal associations between the covarying thermocline and wind stress curl anomaly fields from SVD analysis are consistent with the findings of Miller et al. (1998) and Deser et al. (1999) based upon different techniques and periods of record, and support their physical interpretation in terms of simple wind-driven Sverdrup dynamics. In particular, Sverdrup theory states that at any given latitude, the geostrophic transport streamfunction is proportional to the zonally integrated wind stress curl westward from the eastern boundary. Thus, one expects a westward-intensified pattern of a deep (shallow) thermocline anomaly, or equivalently, a positive (negative) temperature perturbation at a fixed depth within the thermocline, at the latitude where the zonal integral of the wind stress curl anomaly is negative (positive). Miller et al. and Deser et al. have demonstrated that the spatial patterns of wind stress curl and thermocline temperature anomalies in Fig. 16 are consistent with Sverdrup theory. They also show that the change in eastward transport of the Kuroshio Current Extension from the 1970s to the 1980s (inferred from depth-integrated thermal anomalies) is largely accounted for by the change in Sverdrup transport inferred from the wind stress curl field. Deser et al. (1999) suggest that the observed 4–5-yr delay between thermocline variations at the western boundary and basin-scale wind stress curl changes is indicative of the role of baroclinic Rossby waves in the dynamical adjustment of the wind-driven gyre circulation. A detailed investigation of the transient adjustment process in the model simulation is left to future work.

4. Summary and discussion

Interannual variance of observed temperatures within the main thermocline (200–400-m depth) is most strongly pronounced in the western Pacific along the edges of the subtropical gyres in both hemispheres, with typical amplitudes ranging from 0.1 to 1.0 K^2. The two observational analyses agree closely, although the variability is generally weaker in SIO compared to WOA98. In addition, temperature fluctuations from the SIO archive in the southwest tropical Pacific prior to 1980 exhibit unrealistically small amplitudes. Overall, the model simulates well the spatial patterns and magnitudes of subsurface temperature variability. The main discrepancies occur along the Kuroshio Current Extension where the model substantially underestimates the variability at 400-m depth (the variance maximum is also displaced northward by several degrees of latitude compared to observations), and along the equatorward edge of the northern subtropical gyre where the model variance at 200 m is substantially greater than observed. We speculate that the former is related to differences between the climatology of the model and observations (in particular, the more northerly position and weaker intensity of the climatological Kuroshio Current Extension), and that the latter is associated in part with erroneously large wind stress curl variance directly south of the Hawaiian Islands in the NCEP reanalyses. The vertical structure of subsurface temperature variance along the equatorward flanks of the northern and southern subtropical gyres exhibits a localized maximum at the depth of the strongest mean vertical temperature gradient (150–200 m) in both the model and observations. In contrast, the vertical structure for the poleward flank of the northern subtropical gyre (Kuroshio Current Extension) is nearly uniform within the upper 400 m, albeit more so in the observations than in the model.

The dominant association between thermocline variability and wind stress curl forcing in the North Pacific is nonlocal and noncontemporaneous. Specifically, the strongest coupling in both the model and observations occurs between a westward-intensified pattern of 400-m temperature anomalies along the Kuroshio Current Extension and a basinwide pattern of wind stress curl fluctuations 4 yr earlier. The spatial patterns and temporal associations between the covarying thermocline and wind stress curl anomaly fields are consistent with earlier findings by Miller et al. (1998) and Deser et al. (1999), and support their physical interpretation in terms of Sverdrup balance.

In the western tropical Pacific, local wind stress curl fluctuations play an important role in driving thermocline anomalies. In both the model and observations, approximately half of the interannual temperature variance within the main thermocline of the NW and SW Tropics is accounted for by wind-induced Ekman pumping anomalies one season earlier. In addition to local wind forcing, westward-propagating disturbances (e.g., Rossby waves) forced by Ekman pumping anomalies farther east contribute to interannual thermocline variations within the NW Tropics domain; no evidence was found for westward-moving disturbances in the latitude band of the SW Tropics (6°–16°S). Capotondi and Alexander (2001) quantify the relative contributions of local Ekman pumping and Rossby waves for the simulated thermocline variations in the latitude band 12°–14°N as a function of frequency. They find that at low frequencies (decadal and longer), the remote influence of Rossby waves is stronger than that of local Ekman pumping near the western boundary. A similar analysis remains to be conducted for the observed thermocline anomalies. The high-frequency fluctuations of thermocline temperature anomalies in the NW Tropics, as given by their one-season time tendencies, exhibit close quantitative agreement with those induced by local contemporaneous Ekman pumping variations; in the SW Tropics, Ekman pumping underestimates the one-season time tendencies of thermocline temperatures by approximately a factor of 2.

A striking discrepancy was found between the simulated and observed thermocline temperature anomalies in the NW Tropics during the late 1970s. This discrepancy was traced to an erroneous feature in the NCEP wind stress curl product over the NE Tropics. The reasons for the erronous NCEP wind stress curl anomaly are not clear, but we note that the tropical eastern Pacific is a region of sparse surface measurements and one where winds at the surface and those near the top of the boundary layer, as indicated by low-level cloud motion, are often decoupled (cf. Deser and Wallace 1990). Thus, if the NCEP product infers surface winds in this region largely from low cloud motions and other parameters related to winds above the boundary layer (see Kalnay et al. 1996), then it is not surprising that there may be differences between the actual surface wind anomalies and those in the NCEP reanalyses. This discrepancy highlights the need to verify models with a range of observational datasets, in analogy with the procedure used here for subsurface temperature variability. It also highlights the need for a simple dynamical framework for understanding and assessing the realism of both the model and observations.

Acknowledgments. The first author gratefully acknowledges financial support from the NOAA Postdoctoral Program in Climate and Global Change, administered by the University Corporation for Atmospheric Research. We thank Drs. Peter Gent, Bill Large, Scott Doney, Michael Alexander, and Antonietta Capotondi for useful discussions during the course of this work. Helpful comments from two anonymous reviewers led to improvements in the manuscript. NCEP reanalysis data were provided by the NOAA–CIRES Climate Diagnostics Center, Boulder, Colorado.

REFERENCES

Antonov, J., S. Levitus, T. Boyer, M. Conkright, T. O'Brien, and C. Stephens, 1998: *Temperature of the Pacific Ocean.* Vol. 2, *World Ocean Atlas 1998,* NOAA Atlas NESDIS 28, 166 pp.

Barnes, S. L., 1973: Mesoscale objective map analysis using weighted time series observations. NOAA Tech. Memo. ERL NSSL-62, 60 pp.

Bretherton, C. S., C. Smith, and J. M. Wallace, 1992: An intercomparison of methods for finding coupled patterns in climate data. *J. Climate,* **5,** 541–560.

Capotondi, A., and M. A. Alexander, 2001: Rossby waves in the tropical North Pacific and their role in decadal thermocline variability. *J. Phys. Oceanogr.,* **31,** 3496–3515.

Chelton, D. B., and M. G. Schlax, 1996: Global observations of oceanic Rossby waves. *Science,* **272,** 234–238.

Delcroix, T., and C. Henin, 1989: Mechanisms of subsurface thermal structure and sea surface thermohaline variabilities in the southwestern tropical Pacific during 1975–85. *J. Mar. Res.,* **47,** 777–812.

Deser, C., and J. M. Wallace, 1990: Large-scale atmospheric circulation features of warm and cold episodes in the tropical Pacific. *J. Climate,* **3,** 1254–1281.

——, and M. S. Timlin, 1997: Atmosphere–ocean interaction on weekly timescales in the North Atlantic and Pacific. *J. Climate,* **10,** 393–408.

——, M. A. Alexander, and M. S. Timlin, 1996: Upper-ocean thermal variations in the North Pacific during 1970–1991. *J. Climate,* **9,** 1840–1855.

——, ——, and ——, 1999: Evidence for a wind-driven intensification of the Kuroshio Current extension from the 1970s to the 1980s. *J. Climate,* **12,** 1697–1706.

Gent, P. R., and J. C. McWilliams, 1990: Isopycnal mixing in ocean circulation models. *J. Phys. Oceanogr.,* **20,** 150–155.

——, F. O. Bryan, G. Danabasoglu, S. C. Doney, W. R. Holland, W. G. Large, and J. C. McWilliams, 1998: The NCAR Climate System Model global ocean component. *J. Climate,* **11,** 1287–1306.

Giese, B. S., and J. A. Carton, 1999: Interannual and decadal variability in the tropical and midlatitude Pacific Ocean. *J. Climate,* **12,** 3402–3418.

Gill, A. E., 1982: *Atmosphere–Ocean Dynamics.* Academic Press, 662 pp.

Harrison, D. E., 1989: On climatological monthly mean wind stress and wind stress curl fields over the World Ocean. *J. Climate,* **2,** 57–70.

Hautala, S. L., D. H. Roemmich, and W. J. Schmitz, 1994: Is the North Pacific in Sverdrup balance along 24°N? *J. Geophys. Res.,* **99,** 16 041–16 052.

Hellerman, S., and M. Rosenstein, 1983: Normal monthly wind stress over the world ocean with error estimates. *J. Phys. Oceanogr.,* **13,** 1093–1104.

Kagimoto, T., and T. Yamagata, 1997: Seasonal transport variations of the Kuroshio: An OGCM simulation. *J. Phys. Oceanogr.,* **27,** 403–418.

Kalnay, E., and Coauthors, 1996: The NCEP/NCAR 40-Year Reanalysis Project. *Bull. Amer. Meteor. Soc.,* **77,** 437–471.

Kessler, W. S., 1990: Observations of long Rossby waves in the northern tropical Pacific. *J. Geophys. Res.,* **95,** 5183–5217.

Large, W. G., J. C. McWilliams, and S. C. Doney, 1994: Oceanic vertical mixing: A review and a model with a nonlocal boundary layer paremeterization. *Rev. Geophys.,* **32,** 363–403.

Legler, D. M., and J. J. O'Brien, 1988: Tropical Pacific wind stress analysis for TOGA. *IOC Time Series of Ocean Measurements.* IOC Tech. Series 33, Vol. 4, UNESCO.

Levitus, S., T. Boyer, M. Conkright, D. Johnson, T. O'Brien, J. Antonov, C. Stephens, and R. Gelfeld, 1998: *Introduction.* Vol. 1, *World Ocean Database 1998,* NOAA Atlas NESDIS 18, 346 pp.

Miller, A. J., D. R. Cayan, and W. B. White, 1998: A westward-intensified decadal change in the North Pacific thermocline and gyre-scale circulation. *J. Climate,* **11,** 3112–3127.

Milliff, R. F., and J. Morzel, 2001: The global distribution of the time-average wind stress curl from NSCAT. *J. Atmos. Sci.,* **58,** 109–131.

Niiler, P. P., and C. J. Koblinsky, 1985: A local time-dependent Sverdrup balance in the eastern North Pacific Ocean. *Science,* **229,** 754–756.

Qiu, B., and M. Joyce, 1992: Interannual variability in the mid- and low-latitude western North Pacific. *J. Phys. Oceanogr.,* **22,** 1062–1079.

Sverdrup, H., 1947: Wind-driven currents in a baroclinic ocean; with application to the equatorial currents of the eastern Pacific. *Proc. Natl. Acad. Sci.,* **33,** 318–326.

Tourre, Y. M., and W. B. White, 1995: ENSO signals in global upper-ocean temperature. *J. Phys. Oceanogr.,* **25,** 1317–1332.

Trenberth, K. E., 1984: Some effects of finite sample size and persistence on meteorological statistics. Part I: Autocorrelations. *Mon. Wea. Rev.,* **112,** 2359–2368.

——, W. G. Large, and J. G. Olsson, 1990: The mean annual cycle in global ocean wind stress. *J. Phys. Oceanogr.,* **20,** 1742–1760.

White, W. B., 1995: Design of a global observing system for gyre-scale upper ocean temperature variability. *Progress in Oceanography,* Vol. 36, Pergamon, 169–217.

Wunsch, C., and D. Roemmich, 1985: Is the North Atlantic in Sverdrup balance? *J. Phys. Oceanogr.,* **15,** 1876–1880.

Xie, S.-P., T. Kunitani, A. Kubokawa, M. Nonaka, and S. Hosoda, 2000: Interdecadal thermocline variability in the North Pacific for 1958–97: A GCM simulation. *J. Phys. Oceanogr.,* **30,** 2798–2813.